

Supplementary material for
Experimental and CFD evaluation of Ozone Efficacy against
Coronavirus and Enteric Virus Contamination on Public Transport
Surfaces.

Irene Falcó¹, Walter Randazzo¹, Gloria Sánchez¹

Jose Vilarroig², Javier Climent², Sergio Chiva³

A. Chica⁴, J. Navarro-Laboulais^{5*}

¹Department of Preservation and Food Safety Technologies, Institute of Agrochemistry and Food Technology, IATA-CSIC, Av. Agustín Escardino 7, Paterna, 46980, Valencia, Spain

²Hydrodynamic and Environmental Services, Av. del Mar, 53, 12003, Castellón, Spain

³ Universitat Jaume I, Department of Mechanical Engineering and Construction, Av. Vicent Sos Baynat, s/n, 12071 Castellón, Spain

⁴Instituto de Tecnología Química. Universitat Politècnica de València-Consejo Superior de Investigaciones Científicas. Avd. de Los Naranjos S/n, 46022, Valencia, Spain

⁵ Department of Chemical and Nuclear Engineering. Universitat Politècnica de València. Camino de Vera s/n, 46022 Valencia, Spain

* Corresponding author

1. Single phase model used

RANS equations have been used to model the single-phase flow regime. The turbulence models aim to solve a modified set of transport equations by introducing averaged and fluctuating components. For example, a velocity U_i may be divided into an average component, \bar{U}_i , and a time varying component, u_i . The averaged component is given by:

$$\bar{U}_i(t) = \frac{1}{\Delta t} \int_t^{t+\Delta t} U_i(t) dt \quad (S1)$$

where Δt is a time scale that is large relative to the turbulent fluctuations, but small relative to the time scale to which the equations are solved. For compressible flows, the averaging is weighted by density (Favre-averaging), but for simplicity, the following presentation assumes that density fluctuations are negligible. For transient flows, the equations are ensemble averaged. This allows the averaged equations to be solved for transient simulations too.

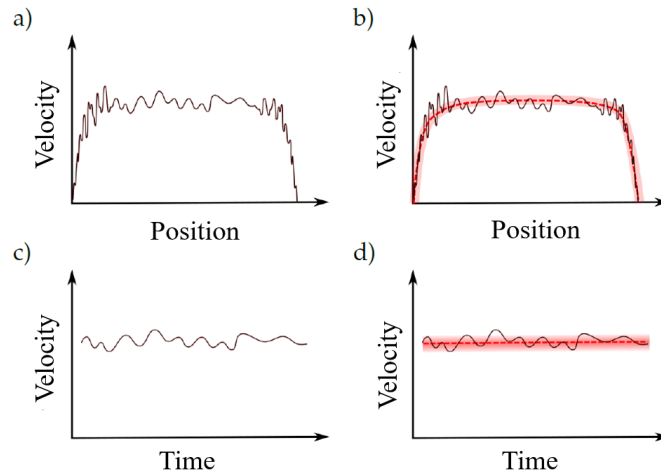


Figure S1. Decomposition of Reynolds in a pipe.

This type of information can be obtained by entering the so-called decomposition of Reynolds. As an example, Fig. 1S(a) illustrates the radial profile of instantaneous velocity in a tubular flow. The velocity is maximum in the centre and zero at the wall of the pipe. The profile is not smooth as it is in the laminar case, but there are small oscillations very close to each other. According to this decomposition, this field can be split into two fields as appears in Fig. 1S(b), that is, in a field of soft spatial variation (dashed line) and a field that expresses the amplitude of

the oscillations (degraded). In the same way, Fig. 1S(c) illustrates the evolution of velocity at the central point of the pipe. The velocity does not remain constant in time. Although the pumping power can be considered as constant, it presents small temporary fluctuations. The decomposition of Reynolds takes this behaviour as shown in Fig. 1S(d), that is, as a field of average velocity (dashed line) and a field that determines the amplitude of fluctuations (degraded).

Substituting the averaged quantities into the original transport equations results in the Reynolds averaged equations given below. In the following equations, the bar is dropped for averaged quantities, except for products of fluctuating quantities.

Mass Conservation

$$\frac{\delta \rho}{\delta t} + \text{div}(\rho U_i) = 0 \quad (\text{S2})$$

Linear Momentum Conservation

$$\begin{aligned} \frac{\delta(\rho U_1)}{\delta t} + \text{div}(\rho U_1 U_1) \\ = -\frac{\delta p}{\delta x_1} + \text{div}(\tau \text{ grad} U_1) \\ + \left[-\frac{\delta(\rho \overline{u_1^2})}{\delta x_1} - \frac{\delta(\rho \overline{u_1 u_2})}{\delta x_2} - \frac{\delta(\rho \overline{u_1 u_3})}{\delta x_3} \right] + S_{Mx_1} \end{aligned} \quad (\text{S3})$$

$$\begin{aligned}
& \frac{\delta(\rho U_2)}{\delta t} + \text{div}(\rho U_2 U_1) \\
&= -\frac{\delta p}{\delta x_2} + \text{div}(\tau \text{ grad} U_2) \\
&+ \left[-\frac{\delta(\rho \overline{u_1 u_2})}{\delta x_1} - \frac{\delta(\rho \overline{u_2^2})}{\delta x_2} - \frac{\delta(\rho \overline{u_2 u_3})}{\delta x_3} \right] + S_{Mx_2}
\end{aligned}$$

$$\begin{aligned}
& \frac{\delta(\rho U_3)}{\delta t} + \text{div}(\rho U_3 U_1) \\
&= -\frac{\delta p}{\delta x_3} + \text{div}(\tau \text{ grad} U_3) \\
&+ \left[-\frac{\delta(\rho \overline{u_1 u_3})}{\delta x_1} - \frac{\delta(\rho \overline{u_2 u_3})}{\delta x_2} - \frac{\delta(\rho \overline{u_3^2})}{\delta x_3} \right] + S_{Mx_3}
\end{aligned}$$

where τ is the molecular stress tensor (including both normal and shear components of the stress).

The continuity equation has not been modified but the momentum and scalar transport equations contain turbulent flux terms additional to the molecular diffusive fluxes. These are the Reynolds stresses, $\overline{u_i u_j}$. These terms stand up from the nonlinear convective term in the un-averaged equations. They reproduce the convective transport due to turbulent velocity fluctuations which will act to enhance mixing over and above that caused by thermal fluctuations at the molecular scale. Consequently, at high Reynolds numbers, turbulent velocity fluctuations the turbulent fluxes are much larger than the molecular fluxes. The additional variable Φ may be divided into an average component, $\overline{\Phi}$, and a time varying component, φ . After dropping the bar for averaged quantities, except for products of fluctuating quantities, the additional variable equation becomes

Energy conservation

$$\begin{aligned}
 & \frac{\delta(\rho\Phi)}{\delta t} + \text{div}(\rho U_i \Phi) \\
 & = \text{div}(\Gamma \text{grad} \Phi) \\
 & + \left[-\frac{\delta(\rho \overline{u_1 \phi})}{\delta x_1} - \frac{\delta(\rho \overline{u_2 \phi})}{\delta x_2} - \frac{\delta(\rho \overline{u_3 \phi})}{\delta x_3} \right] + S_\phi
 \end{aligned} \tag{S4}$$

52 where $\rho \overline{u_j \phi}$ is the Reynolds flux.

53 To better understand the effect of each of the parameters below, it is indicated which term
 54 corresponds to each effect. For the case of the conservation equation of the moment of the X
 55 coordinate:

The diagram shows the momentum conservation equation for the x_1 coordinate, with terms grouped and labeled as follows:

- Local acceleration:** $\frac{\delta(\rho U_1)}{\delta t}$
- Convective term:** $\text{div}(\rho U_1 U_1)$
- Pressure gradient:** $-\frac{\delta p}{\delta x_1}$
- Reynolds Stress (Turbulence):** $\text{div}(\tau \text{grad} U_1)$
- Diffusive term:** $\text{div}(\tau \text{grad} U_1)$
- Source term:** S_{Mx_1}

The equation is written as:

$$\frac{\delta(\rho U_1)}{\delta t} + \text{div}(\rho U_1 U_1) = -\frac{\delta p}{\delta x_1} + \text{div}(\tau \text{grad} U_1) + \left[-\frac{\delta(\rho \overline{u_1^2})}{\delta x_1} - \frac{\delta(\rho \overline{u_1 u_2})}{\delta x_2} - \frac{\delta(\rho \overline{u_1 u_3})}{\delta x_3} \right] + S_{Mx_1} \tag{S5}$$

56 **2. Numerical Resolution**

57 The laws of conservation: conservation of mass, momentum and energy are applied to reach at
 58 partial differential equations (PDE) which mathematically represent the functional relationship
 59 between the influencing state variables in the domain of analysis. There are different numerical
 60 methods available for solving these PDEs.

61 A finite volume method (FVM) discretization is based on an integral form of the partial
 62 differential equations (PDE) to be solved (e.g. conservation of mass, momentum, or energy).

63 The PDEs are written in a form which can be solved for a given finite volume (or cell). The

computational domain is discretized into finite volumes where for every volume the equations are solved. The resulting system of equations usually involves fluxes of the conserved variable, and thus the calculation of fluxes is very important in FVM. It provides a discrete solution, the properties are calculated for every cell instead of a node. Based on the integral form of conservation laws and can handle discontinuities in solutions, in simple terms, what comes in, must go out. It is efficient in solving fluid flow problems.

ANSYS CFX software supports arbitrary mesh topologies, including hexahedral, tetrahedral, wedge and pyramid elements. It uses a unique hybrid finite-element/finite-volume approach to discretizing Navier-Stokes equations. As a finite volume method, it satisfies strict global conservation by enforcing local conservation over control volumes that are constructed around each mesh vertex or node. The finite element methodology is used to describe the solution variation (needed for various surface fluxes and source terms) within each element. Advection fluxes are evaluated using a high-resolution scheme that essentially is second-order accurate and bounded. For transient flows, an implicit second order accurate time differencing scheme is used.

In our case, from the several different discretization methods that are used in CFD codes, the one on which CFX is based is the finite volume technique. In this technique, the region of interest is divided into small sub-regions, called control volumes. The equations are discretized and solved iteratively for each control volume. As a result, an approximation of the value of each variable at specific points throughout the domain can be obtained.

In ANSYS® CFX, Scalable Wall Functions are used for all turbulence models based on the ϵ -equation. For $(k-\omega)$ based models (including the SST model), an Automatic near-wall treatment method is applied overcome one of the major drawbacks of the standard wall function approach in that they can be applied on arbitrarily fine meshes. If one is not interested in the details of the boundary layer, then it may not be worth fully resolving it. However, if the aim is to examine with detail the boundary layer for which a very fine near-wall mesh has been produced, then one

should use the SST model with Automatic near-wall treatment to take advantage of the additional effect in the viscous sublayer.

The flows have certain properties in common near the walls (indicated by both experimental measurements and DNS simulations), regardless of the geometry or its average velocity.

3. Meshing

The mesh selected for the simulation was developed following the CFX Best Practices Guide for Numerical Accuracy (see Ref. [41] in the manuscript). A tetrahedral dominant mesh was performed to calculate the simulations, which guarantee the accuracy and stability of the numerical computation by the mesh quality parameters (aspect ratio and skewness).

The maximum node size used in the domain has been 100 mm. The largest nodes have remained in the central zone where the velocities do not present large gradients. However, in the seating areas, as well as in the handrails, node sizes of 20 mm have been used (while, in the walls of the tram, as well as in the windows, the size used has been 80 mm).



Figure S2. General view of the mesh of the entire domain

In addition, the distance to the first node between any of the model walls is 1-5 mm to guarantee a good calculation of the reactions in these critical areas, for this it has been necessary to carry out a 2-layer meshing as shown in the Figure S3 right.

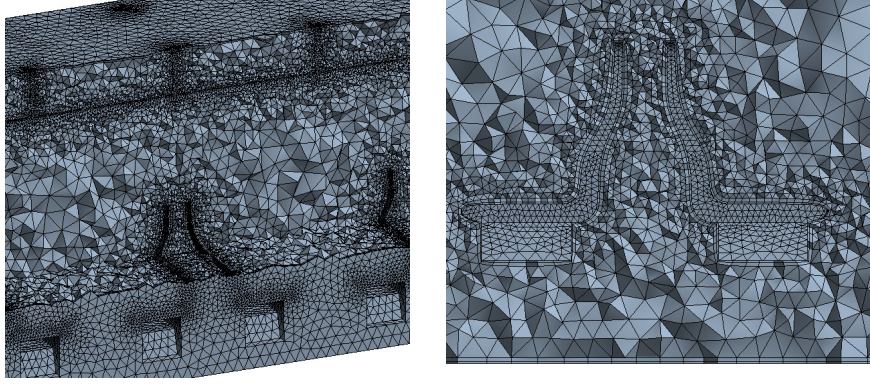


Fig. S3. Detail of the mesh on the handrails and seats (left) and detail of the mesh of layers on the surfaces of the seats and walls (right).

Finally, a model with 1.76 million nodes has been obtained which is adequate to obtain precise results in acceptable computational times. The adequacy of the mesh was analyzed using the Courant number. This dimensionless parameter is essential for calculating fluid velocity on surfaces. It represents the quotient between the time interval and the residence time in a finite volume. It serves to guarantee the validity of the results, evaluating the adequacy of the time step selected in the calculation of the simulations in relation to the mesh size and the fluid velocity through it. Values of the order of magnitude of unity are expected.

$$Courant = \frac{\Delta t}{\Delta x/u} = \frac{u \Delta t}{\Delta x}$$

where u is the fluid velocity, Δt is the timestep and Δx is the mesh size. The Courant number calculated in ANSYS CFX is a multidimensional generalization of this expression where the velocity and length scale are based on the mass flow into the control volume and the dimension of the control volume. For explicit CFD methods, the time step must be chosen such that the Courant number is sufficiently small. The details depend on the specific scheme, but it is usually of order unity.

In this work, it is of special importance for the calculation of the reactions of ozone consumption on the surfaces. The results in Figure S4 show values of the Courant below of 5 on more than 90% of the surfaces. It is only slightly higher (5-15) in the areas corresponding to the entrance as the fluid velocity in this area is higher than in the rest. These Courant values guarantee that the results obtained from the simulations using this mesh are correct.

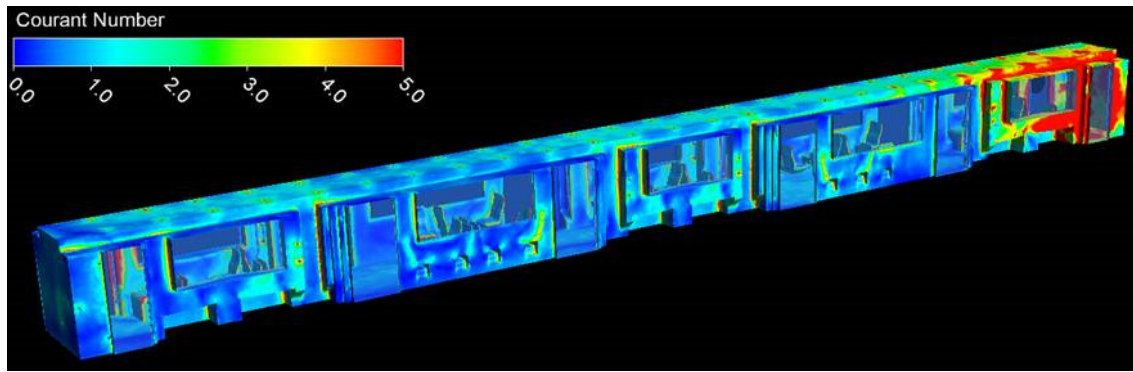


Fig. S4. Courant distribution over the surfaces of the domain.

The ozone surface removal on material surfaces depends on the local ozone concentration adjacent to the surface. The main limitation of CFD modelling to calculate the sink surface deposition flux correctly is that extremely fine meshes near the surfaces are required, values of $1\text{E-}8$ for the distance from the surface to the first calculation node. Because of this, the model proposed by Sørensen and Weschler (see Ref. [21] in the manuscript) was implemented in the CFD model. It allows the calculation for larger meshes as long as a boundary layer flow prevails over most of the surface area, which is controlled by the distance to the first node, Δy_1 .

Respect to the **convergence procedure** for the calculation, the following three criteria were used: the residual level, the solution imbalances, and monitor points tracking quantities of interest (mainly fluid velocity and ozone concentration) as the analysis progresses. The values were measured experimentally.

In the case of CFX code, one can define monitor points to plot specific variables, to follow the evolution of its value

In our case, the simulation was stopped once the residuals arrived at their defined termination values ($< 1\text{E-}4$), and the monitor points of the Fluid Velocity achieved the adequate stability. Moreover, the value of the imbalances was checked while the simulation was running to ensure the conservation of the variables (ozone concentration) at the end of the run.

4. Residence Time Distribution (RTD), fluid velocity and ozone concentration distributions

The ozone concentration was used as a tracer to monitor the RTD at several monitored points. The concentration of ozone is homogeneous after the 300s pulse (figure S5).

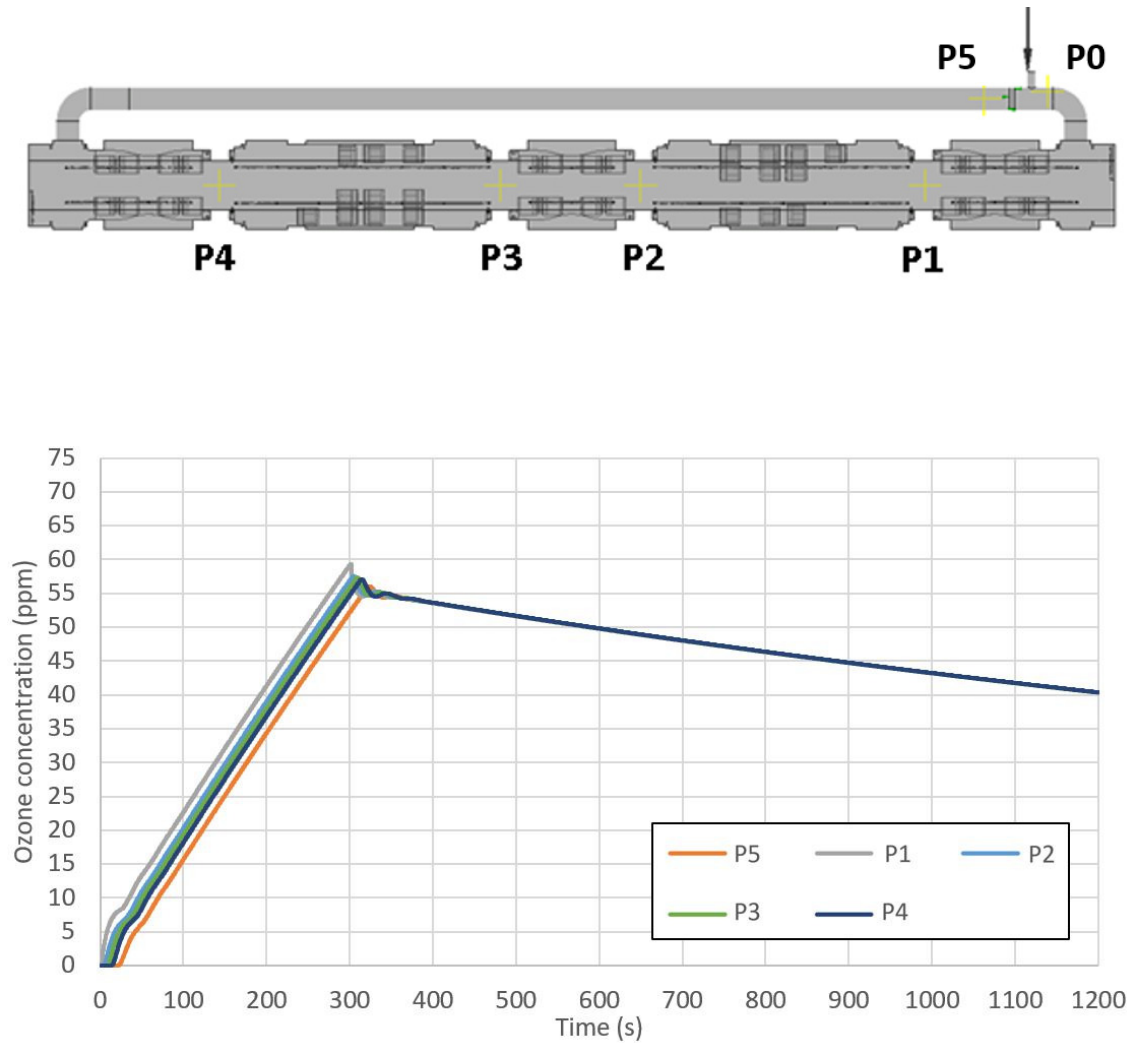


Fig. S5. Virtual monitor points to calculate the ozone concentration distribution.

The lowest fluid velocities were found among seats where the setting is “2-front-2-facing” and which produce a much higher shadow the “1-front-1-facing” setting.

In figure S6, the red volumes show the slow velocity zones (below 0.2 m/s).

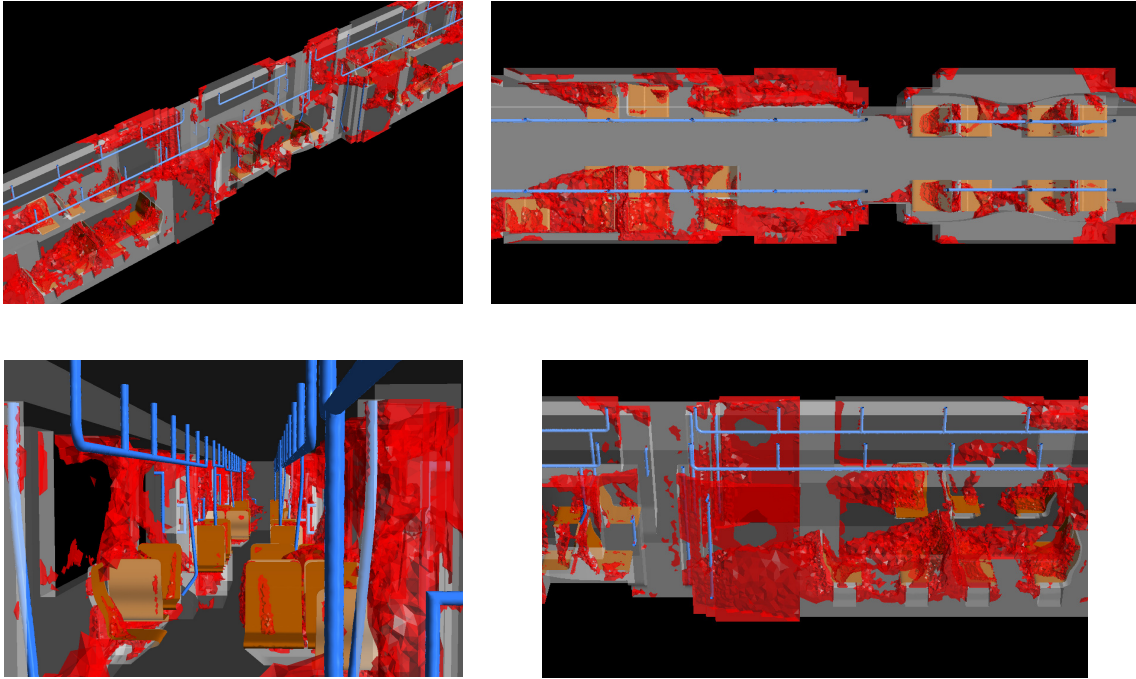


Fig. S6. Detail of the velocity distribution in the planes parallel to the ground at a height of 0.6 meters in the central wagons (left) and in the first wagon (right)

The lowest fluid velocities are concentrated in those points where there are pronounced corners, such as the lateral areas that are just after the bellows that join the different wagons. It is also observed that in the area where there are configurations of 2 seats together, there are shady areas. In the following figures, S7 and S8, the distribution of fluid velocity at these areas is shown in detail as well as the distribution in the first car where the air flow is higher (the entrance):

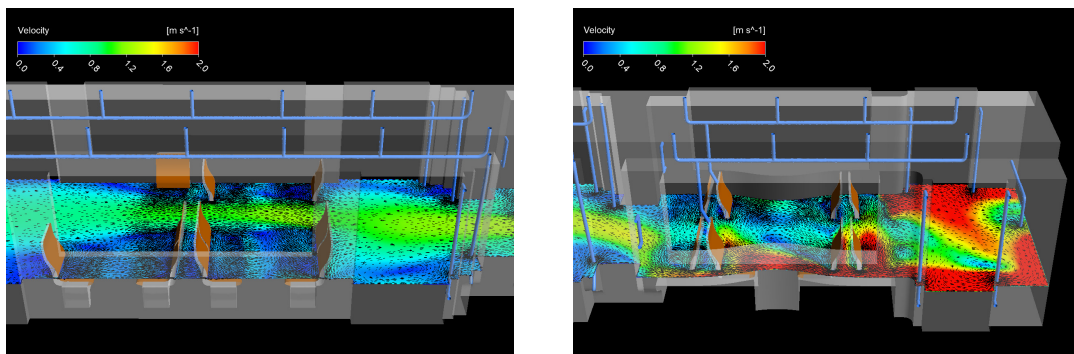


Fig. S7. Detail of the velocity distribution in the planes parallel to the ground at a height of 0.6 meters in the central wagons (left) and in the first wagon (right).

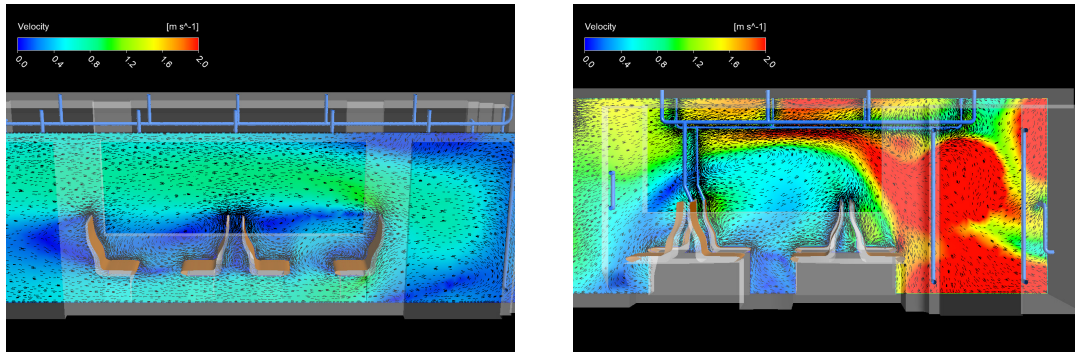


Fig. S8. Detail of the distribution of fluid velocity in the vertical planes that cross the seats in the central wagons (left) and in the first wagon (right).

In Figure S9, it can be seen how this same shielding and swirling effect behind the seats and in the corners also occurs in distributions where there is a single row of seats, but the shadow effect that is produced is much less.

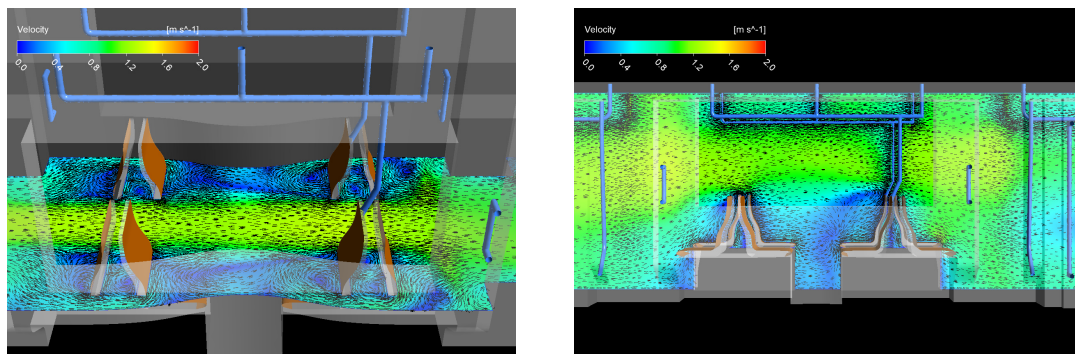


Fig. S9. Detail of the distribution of speeds near the seats in the horizontal (left) and vertical (right) planes of the tram.

As mentioned, the first car where the fan pipe inlet is located has higher air velocity than the rest. Although in this first vehicle the fluid velocity distribution is more heterogeneous, the flow quickly becomes homogeneous as it moves towards the end of the wagon. In next figure, it can be seen how after passing the first car, the fluid velocity is much more homogeneous and do not present notable velocity gradients once the first car has passed (Figure S10).

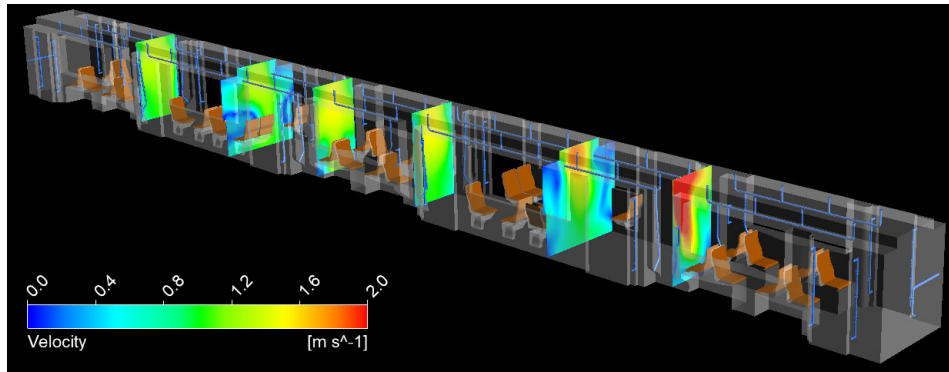


Fig. S10. Distribution of fluid velocity in transverse planes to the tram located at 5, 8, 12, 16, 19 and 23 meters from the entrance.

In these planes, it can also be observed how in the narrowest section, where the bellows is located, the speed is more homogeneous while, right in the central areas of the wagons, the speeds tend to decrease on the sides and increase in the center due to the effect, shielding of the corners and of the seats themselves.

5. Computer Framework The execution time of computation was 49,5 hours with the following equipment:

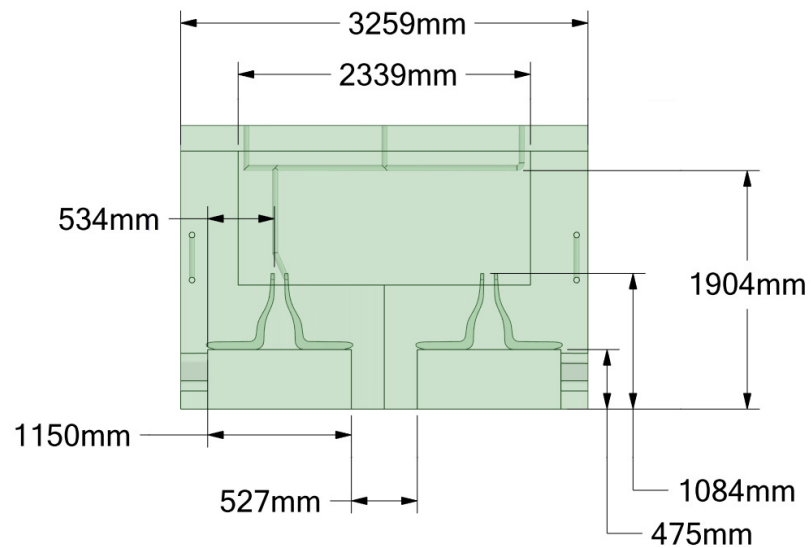
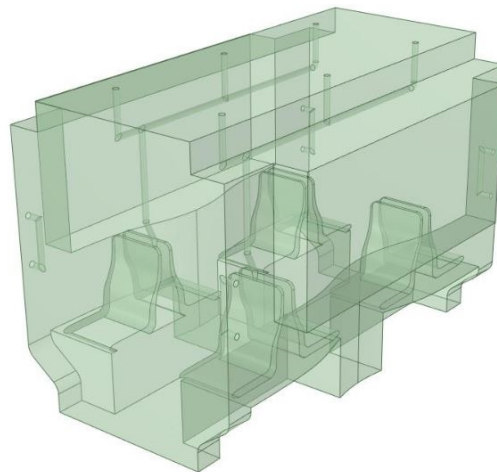
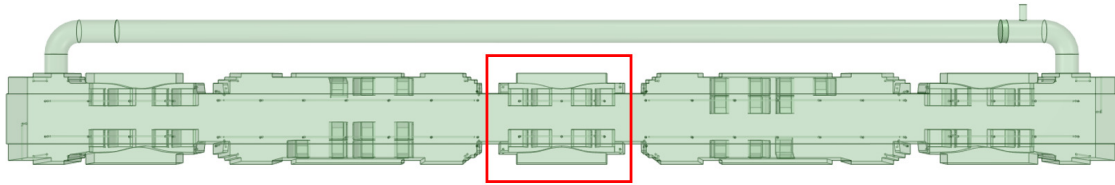
- Processor Intel(R) Core(TM) i7-9800X CPU @ 3.80GHz 3.79 GHz
- 8 Cores
- 64 GB Ram
- 12 TB Physical Storage
- NVIDIA Quadro p2000 GDDR5 5 GB Ram for Post-Processing

Software

- CAD: SpaceClaim v19.2
- CFD: Ansys v19.2

6. Dimensions:

A detailed general view of the CFD domain is shown below with some relevant dimensions (Fig S11) :



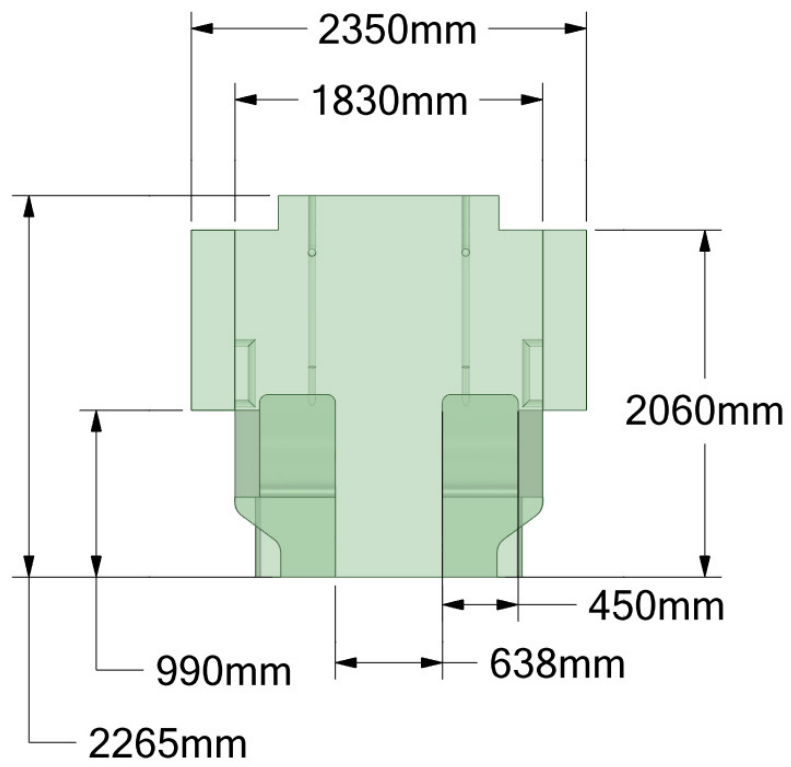


Fig. S11. Dimensions of the domain